

Space-Time Quantum Metasurfaces

Wilton J. M. Kort-Kamp, Abul K. Azad, and Diego A. R. Dalvit*
Los Alamos National Laboratory, Los Alamos, NM 87545, USA

(Dated: January 27, 2021)

Metasurfaces are a key photonic platform to manipulate classical light using sub-wavelength structures with designer optical response. Static metasurfaces have recently entered the realm of quantum photonics, showing their ability to tailor nonclassical states of light. We introduce the concept of space-time quantum metasurfaces for dynamical control of quantum light. We provide illustrative examples of the impact of spatio-temporally modulated metasurfaces in quantum photonics, including the creation of frequency-spin-path hyperentanglement on a single photon and the realization of space-time asymmetry at the deepest level of the quantum vacuum. Photonic platforms based on the space-time quantum metasurface concept have the potential to enable novel functionalities, such as on-demand entanglement generation for quantum communications, nonreciprocal photon propagation for free-space quantum isolation, and reconfigurable quantum imaging and sensing.

The generation, manipulation, and detection of non-classical states of light is at the heart of quantum photonics. As quantum information can be encoded into the different degrees of freedom of a single photon, it is highly desirable to develop photonic platforms that allow to control them while maintaining quantum coherence. Metasurfaces [1, 2] have recently transitioned from the classical to the quantum domain [3] and enabled enhanced light-matter interactions facilitated by the ultrathin subwavelength nature of their constituent scatterers. Spin-orbital angular momentum entanglement of a single photon has been demonstrated [4] using geometrically tailored metasurfaces that induce spin-orbit coupling of light via the Pancharatnam-Berry phase [5], and multi-photon interferences and polarization-state quantum reconstruction has also been achieved in a single geometric phase metasurface [6]. A metasurface-based interferometer has been demonstrated for generating and probing entangled photon states [7], opening opportunities for implementing quantum sensing and metrology protocols using metasurface platforms. Embedded quantum building blocks into arrays of meta-atoms, including quantum dots, semiconductor emitters, and nitrogen-vacancy centers, result in enhanced Purcell factors [8], directional lasing [9], and circularly-polarized single-photon emission [10]. Recently, quantum metasurfaces based on atomic arrays have been proposed [11].

Most demonstrations of metasurfaces in quantum photonics are based on static meta-atoms whose optical properties are determined by their material composition and geometrical design that cannot be changed on demand. A few realizations of active quantum metasurfaces have been reported, for example, for tuning spontaneous emission from a Mie-resonant dielectric metasurface using liquid crystals [12]. However, a fully tailored response requires quantum metasurfaces that can continuously alter their scattering properties simultaneously in space and time. At the classical level, spatio-temporally modulated metasurfaces [13] have been shown to provide that higher degree of control, both by reconfigurable and fully-dynamic tailoring of the optical response of meta-atoms using analog and digital modulation schemes [14, 15].

Here, we put forward the concept of space-time quantum metasurfaces (STQMs) for spatio-temporal control of quantum light. In order to highlight the broad implications of this concept in different areas of quantum science and technology, we discuss two instances of how STQMs operate both at the single-photon and virtual-photon levels. We describe STQM-enabled hyperentanglement [16] manipulation of nonclassical states of light and STQM-induced photon pair generation (Fig. 1) in a process analogue to the dynamical Casimir effect [17].

Results:

We introduce the STQM concept by considering the transmission of a single photon through a metasurface whose meta-atoms are modulated in space and time. The metasurface is composed of identical anisotropic scatterers (Fig. 2a) suitably rotated with respect to each other. The combination of anisotropy and rotation results in circular cross-polarization conversion and a spin-dependent geometric phase distribution $\Psi(\mathbf{r})$ akin to spin-orbit coupling. To minimize photon absorption the metasurface is assumed to be comprised of low-loss dielectric meta-atoms. The spatio-temporal modulation is modeled as a perturbation of the electric permittivity, $\epsilon(\mathbf{r}, t) = \epsilon_{um} + \Delta\epsilon \cos(\Omega t - \Phi(\mathbf{r}))$, where ϵ_{um} is the unmodulated permittivity, $\Delta\epsilon$ the modulation amplitude, Ω the modulation frequency, and $\Phi(\mathbf{r})$ is a “synthetic” phase. Such type of modulation has been recently demonstrated using a heterodyne laser-induced dynamical grating on an amorphous Si metasurface via the nonlinear Kerr effect [18], setting a traveling-wave permittivity perturbation with $\Phi(\mathbf{r}) = \boldsymbol{\beta} \cdot \mathbf{r}$ ($\boldsymbol{\beta}$ is an in-plane momentum “kick”). Note that the geometric phase is fixed by the design of the metasurface while the synthetic phase is reconfigurable on-demand.

STQMs for on-demand entanglement manipulation: The geometry of the dielectric nanoresonator can be tailored so that it has maximal cross-polarized transmission (Fig. 2b) and at the same time so that its Mie electric and magnetic dipolar resonances dominate the

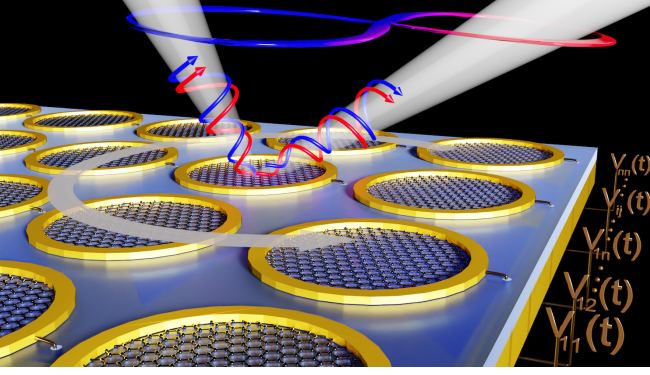


FIG. 1. **Conceptual representation of a space-time quantum metasurface.** A spatio-temporal spinning modulation of graphene nanostructures generates entangled vortex photon pairs out of the quantum vacuum.

optical response of the metasurface. One can then describe the interaction of each Mie resonator with light using the effective Hamiltonian $H_{int} = -\mathbf{p} \cdot \mathbf{E} - \mathbf{m} \cdot \mathbf{B}$ [19, 20], where \mathbf{p} and \mathbf{m} are the electric and magnetic dipole operators and \mathbf{E} and \mathbf{B} are the local quantized electromagnetic fields. Higher-order Mie resonances can be neglected because the transmissivity and reflectivity of the metasurface are well-described by that of an array of electric and magnetic dipoles corresponding to the two lowest Mie multipoles. It is convenient to trace over the nanostructure's degrees of freedom to express the Hamiltonian only in terms of photonic modes by relating dipoles and fields via effective electric α_E and magnetic α_M polarizability tensors (see Supplementary Information for the derivation of the polarizabilities). We show in Fig. 2c the relevant polarizability components for describing the coupling with the normally-incident photon and in Fig. 2d the electric field distributions at the Mie resonance frequencies. The unmodulated Hamiltonian describing cross-polarized transmission has an effective coupling strength $\alpha_{um}^{(cr)}(\omega)$ that is a simple combination of the electric and magnetic polarizabilities (see Methods).

Upon spatio-temporal modulation, the effective polarizabilities adiabatically follow the harmonic driving because the response times of semiconductors (< 100 fs for the nonlinear Kerr response time in amorphous Si) are much faster than THz modulations achievable with all-optical schemes. Hence,

$$\alpha^{(cr)}(\omega; \mathbf{r}, t) = \alpha_{um}^{(cr)}(\omega) + \Delta\alpha^{(cr)}(\omega) \cos(\Omega t - \Phi(\mathbf{r})). \quad (1)$$

We calculate the polarizability modulation amplitude $\Delta\alpha^{(cr)}(\omega)$ from the dependency of transmissivity on permittivity modulation (Fig. 2e). For a 1% permittivity modulation depth the resulting polarizability change is approximately 20%, the increase originating from the strong dispersion of the unmodulated polarizability close to the input frequency. The STQM Hamiltonian $H_1(t)$ is the sum of the unmodulated part plus a modulation

contribution that annihilates the input photon and creates a new one with Doppler-shifted frequency and synthetic phase, in addition to flipping its spin components and adding geometric phases in the same way as the unmodulated part (see Methods). In this work we restrict to unitary evolution as photons do not suffer from severe decoherence problems and absorption is negligible in high-index dielectrics [4].

When the geometric phase is a linear function of the meta-atoms' positions it generates spin-momentum correlations, while a linear synthetic phase creates momentum-frequency correlations. The two correlations are intertwined through momentum and the photon evolves into a state that is hyperentangled in spin, path, and frequency

$$|\psi(t)\rangle = \sum_{p,q} [c_{p,q}^{(R)}(t)|\omega_p; \mathbf{k}_{p,q}; R\rangle + c_{p,q}^{(L)}(t)|\omega_p; \mathbf{k}_{p,-q}; L\rangle], \quad (2)$$

where p are integers, $q = 0, 1$, $R(L)$ denotes right (left) circular polarization, $\omega_p = \omega_{in} + p\Omega$ are harmonics of the input frequency ω_{in} , $\mathbf{k}_{p,q} = \mathbf{k}_{in} + p\boldsymbol{\beta} + q\boldsymbol{\beta}_g$ are in-plane momentum harmonics of the in-plane input wave-vector \mathbf{k}_{in} , and $\boldsymbol{\beta}_g$ is the momentum kick induced by the linear geometric phase. We will denote states in the first term as (p, q, R) and in the second term as $(p, -q, L)$, highlighting that the geometric-phase-induced momentum kicks for right- and left-polarized photons have opposite directions. To calculate the probability amplitudes we consider a normally-incident single-photon pulse and assume modulation frequencies and in-plane momentum kicks much smaller than the input frequency and input wave-vector. Since the dielectric metasurface enables large polarizability modulation amplitudes for modest permittivity variations, it is possible for the input photon to transition to multiple frequency/momentum harmonics during its transit within the metasurface. For input linear polarization, the transition probabilities to states (p, q, R) and $(p, -q, L)$ are identical and are given by

$$|c_{p,q}^{(R/L)}(t)|^2 = \frac{1}{2} \cos^2\left(\frac{\omega_{in} t \alpha_{um}^{(cr)}}{2\hbar P^2}\right) J_p^2\left(\frac{\omega_{in} t \Delta\alpha^{(cr)}}{2\hbar P^2}\right) \quad (3)$$

when p and q have the same parity; for opposite parity the cosine is replaced by a sine. $J_p(x)$ is the Bessel function and probabilities for $\pm p$ are the same (see Supplementary Information for details on the state evolution).

The probability that the output photon is in a given frequency/momentum harmonic as a function of the modulation depth is shown in Fig. 3a. At zero modulation, the output has the same frequency as the input and is approximately an equal superposition of right- and left-polarized geometric-phase-kicked states, with a small overlap with unkicked states due residual co-polarized transmission. As the modulation increases, transitions to only the first few frequency/momentum harmonics occur and a larger amount of the available Hilbert space is explored at large modulation depths. Figure 3b depicts the density matrices of the input (panel (i)) and output photons for different configurations of the STQM, resulting

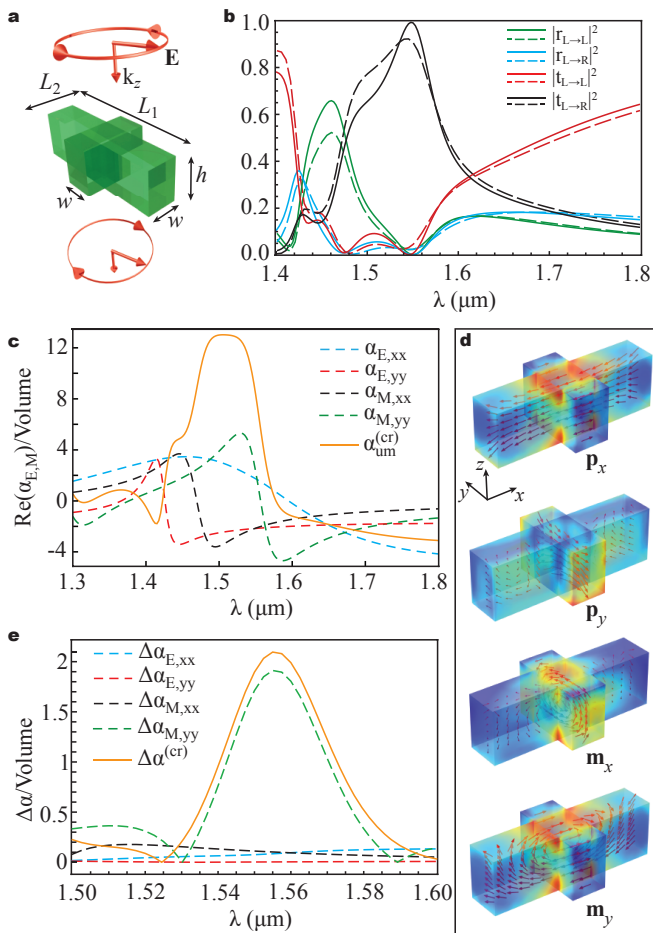


FIG. 2. Effective polarizabilities of all-dielectric space-time quantum metasurfaces. (a) Anisotropic amorphous Si Mie nanocross meta-atom with optimized geometrical parameters for maximal cross-polarization transmission for a normally-incident $\lambda_{in} = 1550$ nm input photon. Parameters are $L_1 = 950$ nm, $L_2 = 435$ nm, $h = 300$ nm, $w = 200$ nm, and square unit cell with period $P = 1200$ nm. (b) Co- and cross-polarized reflectivity and transmissivity for the full metasurface (solid) and electric/magnetic dipole array (dashed). (c) Real parts of the electric and magnetic polarizabilities normalized by the meta-atom volume. Solid line is the effective unmodulated coupling strength for cross-polarized transmission: $\alpha_{um}^{(cr)} \approx 0.6 \mu\text{m}^3$ at the input frequency. (d) Electric field distribution for the two electric and the two magnetic Mie resonances. (e) Polarizability modulation amplitudes for permittivity modulation depth $\Delta\epsilon/\epsilon_{um} = 1\%$. Solid line is the polarizability modulation amplitude for cross-polarized transmission: $\Delta\alpha^{(cr)}/\alpha_{um}^{(cr)} \approx 0.2$ at the input frequency.

in distinct kinds of quantum correlations: (ii) Geometric phase with spatio-temporal modulation off, giving a spin-path entangled output of same frequency as input; (iii-iv) No geometric phase and spatio-temporal modulation on, resulting in frequency-path entangled cross-polarized output; (v-vi) Geometric phase with spatio-temporal modulation on, delivering a frequency-spin-path hyper-

entangled output. It is possible to tailor the modulation depth to completely suppress the contribution of a given harmonic to the output state, as shown in (iv, vi) for the fundamental frequency. Under temporal modulation only, i.e., null synthetic phase (not shown), the output photon is unentangled (hyperentangled) in the absence (presence) of geometric phase. Figure 3c shows the population dynamics of different harmonics while the photon is in-transit inside the STQM. Interestingly, the evolution of populations with and without geometric phase are fundamentally different. Due to spin-orbit coupling the photon undergoes Rabi-flopping between state pairs $(p, 0, R) \leftrightarrow (p, -1, L)$ and $(p, 0, L) \leftrightarrow (p, 1, R)$, and this population exchange cannot take place at zero geometric phase. Unmodulated and modulated polarizabilities control the time-scales of Rabi and synthetic-phase dynamics, respectively.

When both phase distributions are azimuthally varying, i.e., $\Psi(\mathbf{r}) = \ell_g \varphi$, $\Phi(\mathbf{r}) = \ell \varphi$ (ℓ_g and ℓ integers), the input photon becomes hyperentangled in frequency, spin, and orbital angular momentum (OAM) [21]. The state of the photon can be written as in Eq. (2) replacing linear momentum harmonics $\mathbf{k}_{p,q}$ by OAM harmonics $\ell_{p,q} = p\ell + q\ell_g$. Such a rotating synthetic phase could be implemented, e.g., via a heterodyne laser-induced dynamical grating with Laguerre-Gauss petal modes [22, 23] to generate an all-optical spinning perturbation of the meta-atoms' refractive index. As STQMs offer the possibility to reconfigure the synthetic phase on-demand, the question naturally arises as to what happens when the synthetic and geometric phase distributions have utterly different symmetry, for instance one is linear and the other spinning. It is then necessary to expand one phase in terms of a mode basis with symmetries appropriate for the other phase, e.g., plane waves into cylindrical waves (see Supplementary Information for details of mixed-phase STQMs). As the synthetic phase creates frequency-path correlations and the geometric phase spin-OAM correlations, the two correlations are not intertwined and the STQM does not produce hyperentanglement but bipartite entanglement between pairs of degrees of freedom of the single photon. Finally, we mention that all the analysis presented in this section can be extended to other nonclassical inputs, such as two-photon Fock states.

STQMs for tailored photon-generation out of quantum vacuum: Space-time quantum metasurfaces can produce other nonclassical states of light and even induce nonreciprocity [24] on quantum vacuum fluctuations. In addition to the photon-number-conserving Hamiltonian $H_1(t)$ discussed above, STQMs couple to the quantum electromagnetic field via a photon-number-non-conserving Hamiltonian $H_2(t)$ that creates photon pairs out of the quantum vacuum (see Methods). Their frequencies add up to the modulation frequency, $\omega + \omega' = \Omega$, thereby conserving energy, and this process is essentially an analogue of the dynamical Casimir effect (DCE)

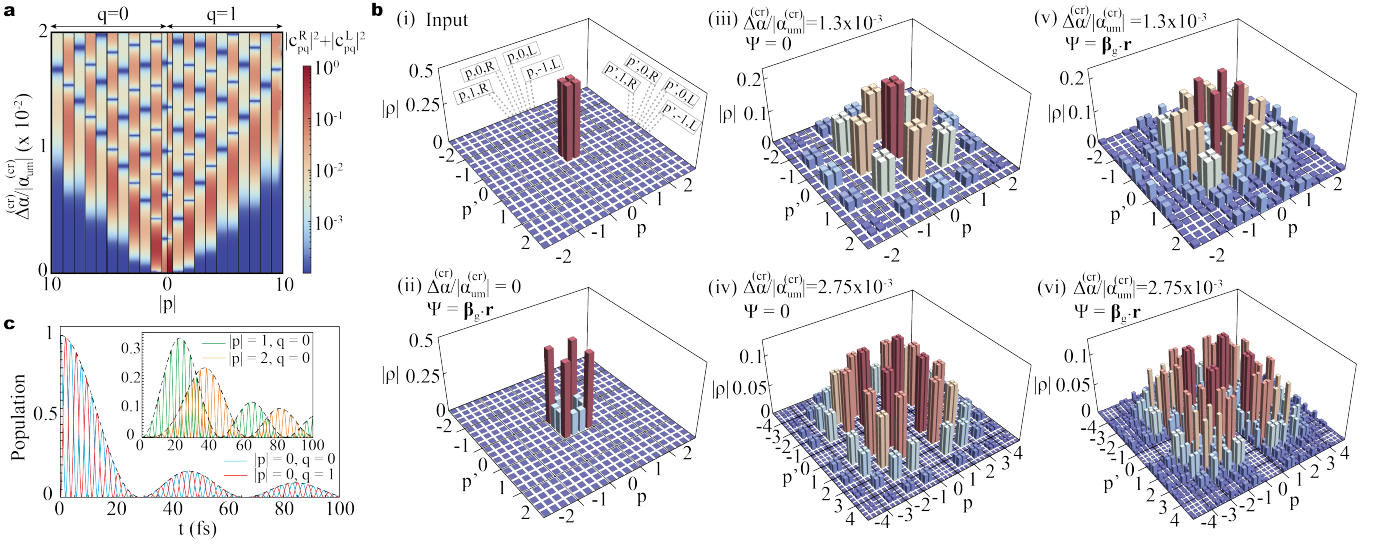


FIG. 3. **Entanglement manipulation with space-time quantum metasurfaces.** (a) Conversion probability into an output photon in frequency harmonic $\omega_{in} + p\Omega$ and momentum harmonic $p\beta + q\beta_g$ versus polarizability modulation depth for the STQM of Fig. 2. (b) Density matrices of input (i) and output photon featuring (ii) spin-path entanglement, (iii-iv) frequency-path entanglement, and (v-vi) frequency-spin-path hyperentanglement. Larger modulation depths result in more harmonics involved in the entangled states (iv) and (vi). (c) Population dynamics of geometric-phase kicked $q = 1$ and unkicked $q = 0$ states for in-transit photon at 0.1 modulation depth, showing Rabi oscillations for the fundamental frequency harmonic. Inset: Rabi dynamics in higher harmonics. Envelopes (dashed black) are the populations of p -harmonics in the absence of geometric phase.

in which an oscillating boundary parametrically excites virtual into real photons [25, 26]. Although the mechanical DCE effect has not been detected because it requires unfeasibly large mechanical oscillation frequencies, various analogue DCE systems have been demonstrated [27–30]. STQMs allow for a novel degree of dynamical control over the quantum vacuum through the synthetic phase: The scattering matrix for the DCE process [31] becomes asymmetric via the spatio-temporal modulation, reflecting that Lorentz reciprocity is broken at the level of quantum vacuum fluctuations.

We first consider the case of the linear synthetic phase (Fig. 4a) and set the geometric phase to zero. Momentum conservation dictates that the emitted photons must have in-plane momenta that add up to the imprinted kick, $\mathbf{k} + \mathbf{k}' = \beta$, and the emitted photons are frequency-path entangled. In Fig. 4b we show the one-photon angular emission distribution for a fixed propagation direction of its twin, indicating how the externally imprinted momentum controls the directivity of the emission process. Figure 4c contains polar plots of the emission distributions for a given circularly-polarized photon pair (see Methods). In the absence of kick, the high-frequency photon can be emitted in any azimuthal direction but it has a maximum polar angle of emission, while no such a constraint exists for the low-frequency photon. As the magnitude of the momentum kick β increases, the distributions undergo intricate changes. The region of allowed emission for the first photon gets deformed when the kick is non-zero and at a critical value of the kick an “island”

of emission appears surrounded by a sea of forbidden emission directions (shaded areas). The island drifts to higher polar angles until it touches the grazing emission line, starts to shrink in size, and finally at $\beta_{max} = \Omega/c$ it collapses to a point and the photon is only emitted parallel to the kick. Far-field emission above that value of the kick is not possible. Regarding the second photon, its emission distribution remains mostly unperturbed until two areas of forbidden emission appear at large polar angles and opposite to the kick direction. The forbidden region grows until it engulfs its allowed emission region and a second island forms (not shown). Finally, it ends up being emitted at a grazing angle but in a direction anti-parallel to the kick. The corresponding spherical plots are shown in Fig. 4d, with emission profiles resembling cone- (dome-) like shapes for the high- (low-) frequency photon and become increasingly distorted as the kick grows. When both photons are emitted with the same frequency, i.e., twin photons, the emission distribution is disk-shaped and gets elongated in a direction parallel to the kick as this increases in magnitude (not shown). The modulation also excites hybrid entangled pairs composed of one photon and one evanescent surface wave (shaded areas in Fig. 4c), and when $\beta > \beta_{max}$ only evanescent modes are created and subsequently decay via non-radiative loss mechanisms.

The two-photon emission rate from an STQM of area A with arbitrary synthetic phase $\Phi(\mathbf{r})$ is

$$\Gamma_{\Phi} = \frac{An_{MS}^2\Omega^4}{512\pi^3c^4} \int_0^{\Omega} d\omega |\Delta\alpha(\omega) + \Delta\alpha(\Omega - \omega)|^2 f_{\Phi}(\omega). \quad (4)$$

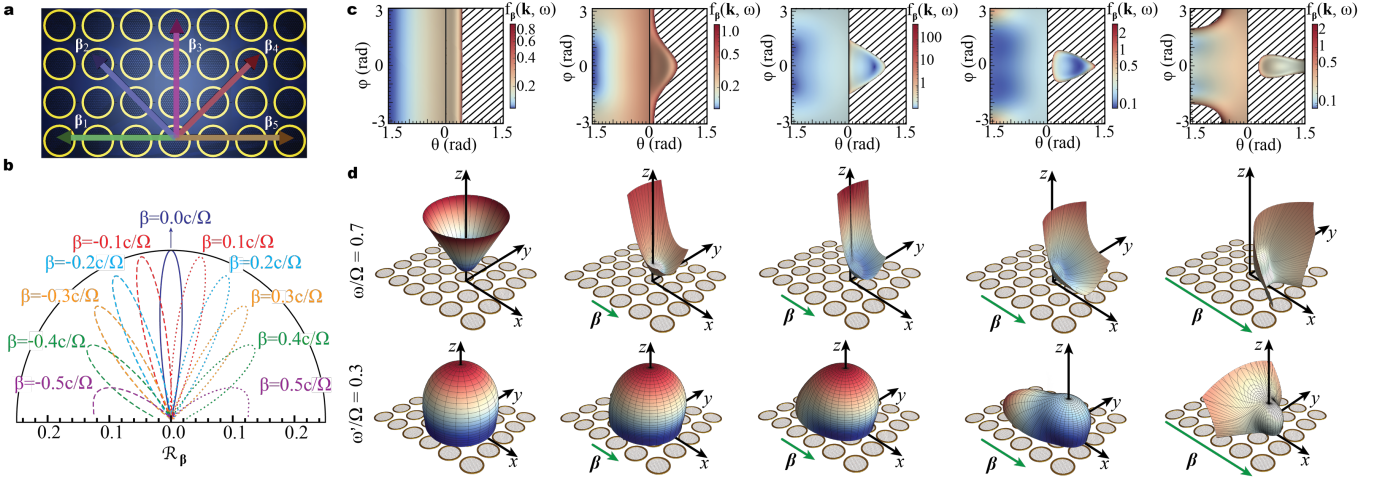


FIG. 4. **Steered quantum vacuum.** (a) A linear synthetic phase is imprinted on a metasurface through a traveling-wave modulation and is tuned on demand (colored arrows) to steer the emitted dynamical Casimir photons. (b) Emission lobes of one photon for varying momentum kick and fixed (vertical) emission direction of its twin. (c) Density polar plots of angular emission spectrum for various $\beta = (0, 0.2, 0.3, 0.38, 0.5)\Omega/c$ from left to right. The areas to the right (left) of the vertical solid line correspond to the angular emission spectrum of the high- (low-) frequency photon in a pair. Frequencies are $\omega/\Omega = 0.7$ and $\omega'/\Omega = 0.3$. Shaded zones correspond to forbidden photon emission directions. Between the two rightmost panels two special events simultaneously happen: the merge of the emission “island” of the high-frequency photon with the grazing line and the birth of forbidden regions for the low-frequency photon. (d) Spherical polar plots for the same panels as in (c).

The rate scales as the square of the meta-atoms number surface density n_{MS} indicating coherent emission of photon pairs. Electro-optical properties of the meta-atoms are contained in the modulated electric polarizability amplitude $\Delta\alpha(\omega)$. The spectral weight function f_{Φ} results from the angular integration of all emission events and is plotted in Fig. 5a for the case of the linear synthetic phase. $f_{\beta}(\omega)$ has a central plateau-like form with sharp edges that at zero kick coalesce into a single logarithmic integrable divergency at the center of the spectrum and corresponds to the emission of twin photons [32]. As the kick grows, the plateau becomes lower and at the maximum allowed kick the spectral weight function vanishes.

STQMs can affect the quantum vacuum in more exotic ways, e.g., a modulation with a spinning synthetic phase “stirs” the vacuum (Fig. 1) and induces angular momentum nonreciprocity [33] at the level of quantum fluctuations. The rotating modulation generates vortex photon pairs that carry angular momenta satisfying $m + m' = \ell$. For $\ell \neq 0$ the average of the Poynting vector over all possible emission events results in a single vortex line along the synthetic spinning axis. Photon pairs are frequency-angular momentum entangled and their quantum correlations could be probed using photo-coincidence detection and techniques based on angular momentum sorting of light [34, 35]. The spectral weight function $f_{\ell}(\omega)$ is reported in Fig. 5b for a finite-radius metasurface, showing plateau-like structures as in Fig. 5a but without the sharp features on the edges, and with decreasing height as the spinning grows. There is a drastic but subtle difference between the two spectral weight functions $f_{\beta}(\omega)$ and $f_{\ell}(\omega)$ that is not apparent in the plots: The

former vanishes beyond the finite kick threshold β_{max} , while there is no finite spinning threshold for the latter. Figures 5c-d show the angular momentum spectra of high- and low-frequency photons in an emitted pair (see Methods). When the STQM does not imprint any spinning, the spectra are symmetric around the peak at $m = 0$, with oppositely twisted photons in each emitted pair. When spinning is imprinted, the two spectra are related as $f_{\ell}(m, \omega) = f_{\ell}(\ell - m, \Omega - \omega)$ and the spectrum for the high- (low-) frequency photon is centered around $m = \ell$ ($m = 0$). This is the angular-momentum equivalent of asymmetric linear momentum emission in Fig. 4d.

Photo-emission rates can be boosted with suitable functional meta-atoms, such as atomically-thin nanostructures made of plasmonic materials that can support highly localized plasmons [36–38] and enable large electric polarizabilities conducive to enhanced coupling of the STQM with the quantum vacuum. As an example, we consider a STQM based on graphene disks whose Fermi energy E_F is spatio-temporally modulated (Fig. 1). Changing the Fermi energy it is possible to tune the plasmonic resonances into the DCE spectral range and to modify the electric polarizability modulation amplitude (inset of Fig. 5e). Furthermore, the use of ultra-high mobility graphene samples minimizes photon absorption and substantially enhances photo-production rates. Figure 5e depicts the spectral rate for a STQM for null synthetic phase at selected Fermi energies, featuring Lorentzian peaks at complementary frequencies. For high-Q resonances the emission rate for arbitrary synthetic phase

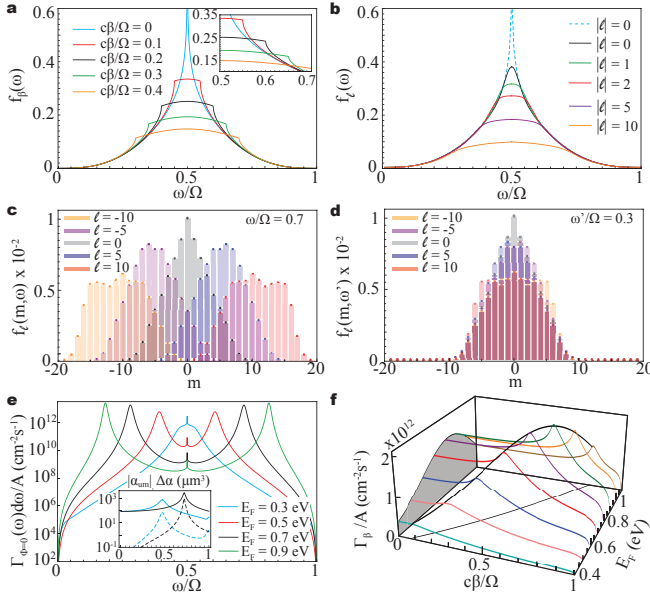


FIG. 5. Photo-emission rates for various synthetic phases. (a) Spectral weight function for linear synthetic phase. Sharp edges of each plateau correspond to the special events of Fig. 4(c). Inset: Crossings responsible for non-monotonicity in (f). (b) Spectral weight function for rotating synthetic phase. Solid lines correspond to a finite radius metasurface ($\Omega R/c = 30$) and dashed line is the $\ell = 0$ case for an infinite metasurface. (c) Angular-momentum spectra for finite radius metasurface for the high-frequency photon. (d) Same as (c) for the low-frequency photon. (e) Spectral photo-production rate for null synthetic phase for a graphene-disk STQM. Inset: unmodulated electric polarizability $\alpha_{um}(\omega)$ (solid) and modulation amplitude $\Delta\alpha(\omega)$ (dashed). (f) Emission rate for linear synthetic phase. The profile on the left shows the rate at null synthetic phase. The black thick curve joins peaks of maximal emission and the thin black curve $c\beta = 2\omega_{res}(E_F) - \Omega$ is its projection on the $\beta - E_F$ plane. The rate decreases non-monotonically to zero at β_{max} . In (e-f) parameters are: $\Omega/2\pi = 10$ THz, $\Delta E_F/E_F = 1\%$, $n_{MS} = 10^3$ mm $^{-2}$, $D = 5$ μ m, and graphene mobility $\mu = 10^4$ cm 2 V $^{-1}$ s $^{-1}$.

can be approximated as

$$\Gamma_{\Phi} \approx g\Omega (An_{MS}^2 D^6 \omega_{res}^4 / c^4) f_{\Phi;res} \left(\frac{\Delta E_F}{E_F} \right)^2 \left(\frac{\Omega}{\gamma} \right)^3 \quad (5)$$

Here, g is a numerical factor determined by the plasmon eigenmode, D the disk diameter, ω_{res} is the plasmonic resonance frequency, $f_{\Phi;res}$ the spectral weight on resonance, $\Delta E_F/E_F$ the Fermi energy modulation depth, and $\Omega/\gamma \gg 1$ with γ the scattering rate of graphene. (see Supplementary Information for the derivation of the polarizability and emission rate). Figure 5f shows the emission rate for the linear synthetic phase as a function of momentum kick and Fermi energy. Giant photon-pair production rates on the order of 10^{12} photons/cm 2 s are obtained at low-THz driving frequencies and modest modulation depths. Conventional electrical doping may

not allow to reach the large Fermi energies where the rate is maximized, but it suffices for exploring the lower Fermi energy region where photon-pairs are already produced in giant numbers. A heterodyne dynamical grating based on ultrafast all-optical THz modulation of graphene conductivity [39] could enable giant and steered photo-pair emission out of the quantum vacuum. Finally, we note that electro-optical ultrafast on-chip graphene modulators [40–42] could potentially be employed to independently bias different STQM graphene pixels with designer temporal delays to implement complex synthetic phases.

Discussion: Metasurfaces are crossing the classical-quantum divide to offer novel possibilities for flat quantum optics and photonics. On the quantum side, they can become an enabler platform for generating and manipulating nonclassical states of light in real time. We uncovered a key property of space-time quantum metasurfaces relevant for potential applications: On-demand reconfiguration of the synthetic phase allows dynamically tunable quantum correlations, enabling to tailor the nature of entanglement depending on the symmetry properties of both geometric and synthetic phases. We also illustrated a second key property of space-time quantum metasurfaces with fundamental relevance: Lorentz non-reciprocity at the deepest level of vacuum fluctuations is attained through joint space and time modulations of optical properties and can be interpreted as an asymmetric quantum vacuum.

Spatio-temporally modulated quantum metasurfaces have the potential to become a flexible photonic platform for generating nonclassical light with designer spatial and spectral shapes, for on-demand manipulation of entanglement for free-space communications, and for reconfigurable sensing and imaging systems. Conversion efficiencies into specific frequency, linear momentum, or orbital angular momentum harmonics for selective quantum information encoding could be enhanced through advanced modulation protocols. Incorporation of quantum matter building blocks into space-time metasurfaces may further expand the possibilities afforded by the proposed platform. As such, space-time quantum metasurfaces can provide breakthrough advances in quantum photonics.

Methods: The effective polarizability tensors $\alpha_E(\omega)$ and $\alpha_M(\omega)$ of the dielectric nanostructure are obtained using a Cartesian multipole expansion [43] of the full-wave simulated electromagnetic field under a plane wave excitation, and computing ratios of the resulting Mie electric and magnetic dipoles to the incident field at the nanostructure's center. The Hamiltonian for the all-dielectric STQM in cross-polarized transmission is

$$H_1(t) = - \sum_{j,\gamma,\gamma'} [\alpha_{um}^{(cr)}(\omega) + \Delta\alpha^{(cr)}(\omega) \cos(\Omega t - \Phi_j)] \times A_{\gamma;j}^* A_{\gamma';j} e^{i(\omega-\omega')t} [e^{i\Psi_j} a_{\gamma,R}^\dagger a_{\gamma',L} + e^{-i\Psi_j} a_{\gamma,L}^\dagger a_{\gamma',R}] + h.c.$$

The sums are over all meta-atoms and field modes, the geometric $\Psi(\mathbf{r})$ and synthetic $\Phi(\mathbf{r})$ phase distributions

are evaluated at the position of the meta-atoms, Ω is the modulation frequency, A_γ , $A_{\gamma'}$ are spatial modes, and $a_{\gamma',L/R}$ and $a_{\gamma,R/L}^\dagger$ are annihilation and creation operators of circularly polarized photons. The unmodulated coupling strength is

$$\alpha_{um}^{(cr)}(\omega) = \text{Re}[\alpha_{E,xx}(\omega) + \alpha_{M,yy}(\omega) - \alpha_{E,yy}(\omega) - \alpha_{M,xx}(\omega)]$$

and $\Delta\alpha^{(cr)}(\omega)$ is the modulation coupling strength obtained by replacing in the above equation each effective polarizability by its respective modulation amplitude.

The Hamiltonian for the all-plasmonic STQM for two-photon emission is

$$H_2(t) = \frac{1}{8} \sum_{j,\gamma,\gamma'} \sum_{\lambda,\lambda'} [\Delta\alpha(\omega - \Omega) + \Delta\alpha(\omega' - \Omega)] \\ \times A_{\gamma;j}^* A_{\gamma';j}^* e^{i\Phi_j} e^{i(\omega+\omega'-\Omega)t} a_{\gamma,\lambda}^\dagger a_{\gamma',\lambda'}^\dagger + h.c.$$

where we neglected multiscattering between meta-atoms [45]. λ, λ' are polarization states of the two photons and $\Delta\alpha(\omega)$ is the modulated electric polarizability amplitude of the meta-atom computed with the plasmon wavefunction formalism [36]. For a graphene disk of diameter D with a high-Q localized bright-mode plasmonic resonance

$$\Delta\alpha(\omega) \approx \frac{\pi^2 a_1^2 \alpha_{fs} c D^2 \Delta E_F}{512 \hbar \Omega^2} \frac{(\gamma/2\Omega)^2}{[(\omega - \omega_{res})/\Omega]^2 + (\gamma/2\Omega)^2}.$$

$\omega_{res}(E_F) = (\alpha_{fs} c E_F / \pi |\xi_1| \hbar D)^{1/2}$ is the resonance frequency of the lowest bright-mode, E_F and ΔE_F are the Fermi energy and its modulation amplitude, α_{fs} is the fine structure constant, $\gamma = ev_F^2 / E_F \mu$ the scattering rate

of graphene, v_F the Fermi velocity, and μ the mobility. The eigenmode coefficients $a_1 = 6.1$ and $\xi_1 = -0.072$ determine $g = 5\pi^4 a_1^4 \xi_1^2 / 2(512)^3$ in Eq. (5). Emission rates are computed with time-dependent perturbation theory. Non-paraxial quantization of the electromagnetic field with angular momentum is employed for the STQM with rotating synthetic phase [44]. The spectral weight functions for the linear and spinning synthetic phases are respectively decomposed into in-plane linear momentum $f_\beta(\mathbf{k}, \omega)$ and angular momentum $f_\ell(m, \omega)$ spectra

$$f_\beta(\omega) = \int d\mathbf{k} (c/\Omega)^2 (1 - |\mathbf{c}\mathbf{k}/\omega|^2)^{-1/2} f_\beta(\mathbf{k}, \omega), \\ f_\ell(\omega) = \sum_m f_\ell(m, \omega).$$

Explicit expressions for these spectra can be found in the Supplementary Information.

Acknowledgements: This work was supported by the DARPA QUEST program. We are grateful to A. Efimov, M. Julian, C. Lewis, M. Lucero, and A. Manjavacas for discussions.

Author Contributions: D.A.R.D. and W. K.-K. conducted the theory work and A. K. A. analyzed experimental feasibility. All authors discussed the findings and contributed to writing the paper.

Competing Interests: The authors declare no competing interests.

*Correspondence: dalvit@lanl.gov

-
- [1] A. V. Kildishev, A. Boltasseva, and V. M. Shalaev, Planar photonics with metasurfaces, *Science* **339**, 1232009 (2013).
- [2] H.-T. Chen, A. J. Taylor, and N. Yu, A review of metasurfaces: physics and applications, *Rep. Prog. Phys.* **79**, 076401 (2016).
- [3] A. S. Solntsev, G. S. Agarwal, and Y. S. Kivshar, Metasurfaces for quantum photonics, arXiv:2007.14722.
- [4] T. Stav, A. Faerman, E. Maguid, D. Oren, V. Kleiner, E. Hasman, and M. Segev, Quantum entanglement of the spin and orbital angular momentum of photons using metamaterials, *Science* **361**, 1101-1104 (2018).
- [5] Z. Bomzon, G. Biener, V. Kleiner, and E. Hasman, Space-variant Pancharatnam-Berry phase optical elements with computer-generated subwavelength gratings, *Opt. Lett.* **27**, 1141-1143 (2002).
- [6] K. Wang, J. G. Titchener, S. S. Kruk, L. Xu, H.-P. Chung, M. Parry, I. I. Kravchenko, Y.-H. Chen, A. S. Solntsev, Y. S. Kivshar, D. N. Neshev, and A. A. Sukhorukov, Quantum metasurface for multiphoton interference and state reconstruction, *Science* **361**, 1104-1108 (2018).
- [7] P. Georgi, M. Massaro, K.-H. Luo, B. Sain, N. Montaut, H. Herrmann, T. Weiss, G. Li, C. Silberhorn, and T. Zentgraf, Metasurface interferometry toward quantum sensors, *Light: Science & Applications* **8**, 70 (2019).
- [8] A. Vaskin, R. Kolkowskia, A. F. Koenderink, and I. Staude, Light-emitting metasurfaces, *Nanophotonics* **8**, 1151-1198 (2019).
- [9] Y.-Y. Xie, P.-N. Ni, Q.-H. Wang, Q. Kan, G. Briere, P.-P. Chen, Z.-Z. Zhao, A. Delga, H.-R. Ren, H.-D. Chen, C. Xu, and P. Genevet, Metasurface-integrated vertical cavity surface-emitting lasers for programmable directional lasing emissions, *Nat. Nanotech.* **15**, 125-130 (2020).
- [10] Y. Kan, S. K. H. Andersen, F. Ding, S. Kumar, C. Zhao, and S. I. Bozhevolnyi, Metasurface-enabled generation of circularly polarized single photons, *Adv. Mater.* **32**, 1907832 (2020).
- [11] R. Bekenstein, I. Pikovski, H. Pichler, E. Shahmoon, S. F. Yelin, and M. D. Lukin, Quantum metasurfaces with atom arrays, *Nat. Phys.* **16**, 676-681 (2020).
- [12] J. Bohn, T. Bucher, K. E. Chong, A. Komar, D.-Y. Choi, D. N. Neshev, Y. S. Kivshar, T. Pertsch, and I. Staude, Active tuning of spontaneous emission by Mie-resonant dielectric metasurfaces, *Nano Lett.* **18**, 3461-3465 (2018).
- [13] A. M. Shaltout, V. M. Shalaev, and M. L. Brongersma, Spatiotemporal light control with active metasurfaces,

- Science **364**, 648 (2019).
- [14] A. E. Cardin, S. R. Silva, S. R. Vardeny, W. J. Padilla, A. Saxena, A. J. Taylor, W. J. M. Kort-Kamp, H.-T. Chen, D. A. R. Dalvit, and A. K. Azad, Surface-wave-assisted nonreciprocity in spatio-temporally modulated metasurfaces, *Nat. Commun.* **11**, 1469 (2020).
- [15] L. Zhang, X. Q. Chen, S. Liu, Q. Zhang, J. Zhao, J. Y. Dai, G. D. Bai, X. Wan, Q. Cheng, G. Castaldi, V. Galdi, and T. J. Cui, Space-time-coding digital metasurfaces, *Nat. Commun.* **9**, 4334 (2018).
- [16] J. T. Barreiro, N. K. Langford, N. A. Peters, and P. G. Kwiat, Generation of Hyperentangled Photons Pairs, *Phys. Rev. Lett.* **95**, 260501 (2005).
- [17] G. T. Moore, Quantum theory of the electromagnetic field in a variable-length one-dimensional cavity, *Journal of Mathematical Physics* **11**, 2679 (1970).
- [18] X. Guo, Y. Ding, Y. Duan, and X. Ni, Nonreciprocal metasurface with space-time phase modulation, *Light: Science & Applications* **8**, 123 (2019).
- [19] A. I. Kuznetsov, A. E. Miroschnichenko, M. L. Brongersma, Y. S. Kivshar, and B. Luk'yanchuk, Optically resonant dielectric nanostructures, *Science* **354**, aag2472 (2016).
- [20] L. Novotny and B. Hecht, *Principles of Nano-Optics* (Cambridge University Press, New York, 2007).
- [21] G. F. Calvo, A. Picón, and E. Bagan, Quantum field theory of photons with orbital angular momentum, *Phys. Rev. A* **73**, 013805 (2006).
- [22] H. J. Eichler, P. Günter, and D. H. Pohl, *Laser induced dynamical gratings* (Springer-Verlag, Heidelberg, 1986).
- [23] D. Naidoo, K. Ait-Ameur, M. Brunel, and A. Forbes, Intra-cavity generation of superpositions of Laguerre-Gaussian beams, *Appl. Phys. B*, **106**, 683–690 (2012).
- [24] D. L. Sounas and A. Alù, Non-reciprocal photonics based on time modulation, *Nat. Photonics* **1**, 774–783 (2017).
- [25] D. A. R. Dalvit, P. A. Maia Neto, and F. D. Mazzitelli, in *Casimir Physics, Lecture Notes in Physics* **834** (eds. D. Dalvit, P. Milonni, D. Roberts, and F. Da Rosa), (Springer, Heidelberg, 2006).
- [26] V. V. Dodonov, Current status of the dynamical Casimir effect, *Physica Scripta* **82**, 038105 (2010).
- [27] C. M. Wilson, G. Johansson, A. Pourkabirian, M. Simoen, J. R. Johansson, T. Duty, F. Nori, and P. Delsing, Observation of the dynamical Casimir effect in a superconducting circuit, *Nature* **479**, 376–379 (2011).
- [28] J.-C. Jaskula, G. B. Partridge, M. Bonneau, R. Lopes, J. Ruauadel, D. Boiron, and C. I. Westbrook, Acoustic Analogue to the Dynamical Casimir Effect in a Bose-Einstein Condensate, *Phys. Rev. Lett.* **109**, 220401 (2012).
- [29] P. Lahteenmaki, G. S. Paraoanu, J. Hassel, and P. J. Hakonen, Dynamical Casimir effect in a Josephson metamaterial, *Proc. Nat. Acad. Sci. USA* **110**, 4234–4238 (2013).
- [30] S. Vezzoli, A. Mussot, N. Westerberg, A. Kudlinski, H. D. Saleh, A. Prain, F. Biancalana, E. Lantz, and D. Faccio, Optical analogue of the dynamical Casimir effect in a dispersion-oscillating fibre, *Commun. Phys.* **2**, 84 (2019).
- [31] M. F. Maghrebi, R. Golestanian, and M. Kardar, Scattering approach to the dynamical Casimir effect, *Phys. Rev. D* **87**, 025016 (2013).
- [32] P. A. Maia Neto and L. A. S. Machado, Quantum radiation generated by a moving mirror in free space, *Phys. Rev. A* **54**, 3420 (1996).
- [33] D. L. Sounas, C. Caloz, and A. Alù, Giant nonreciprocity at the subwavelength scale using angular momentum-biased metamaterials, *Nat. Commun.* **4**, 2407 (2013).
- [34] G. C. Berkhout, M. P. Lavery, J. Courtial, M. W. Beijersbergen, and M. J. Padgett, Efficient Sorting of Orbital Angular Momentum States of Light, *Phys. Rev. Lett.* **105**, 153601 (2010).
- [35] M. Mirhosseini, M. Malik, Z. Shi, and R. W. Boyd, Efficient separation of the orbital angular momentum eigenstates of light, *Nat. Commun.* **4**, 2783 (2013).
- [36] R. Yu, J. D. Cox, J. R. M. Saavedra, and F. J. García de Abajo, Analytical modeling of graphene plasmons, *ACS Photonics* **4**, 3106 (2017).
- [37] F. J. García de Abajo and A. Manjavacas, Plasmonics in atomically thin materials, *Faraday Discuss.* **178**, 87–1073548 (2015).
- [38] Y. Muniz, A. Manjavacas, C. Farina, D. A. R. Dalvit, and W. J. M. Kort-Kamp, Two-Photon Spontaneous Emission in Atomically Thin Plasmonic Nanostructures, *Phys. Rev. Lett.* **125**, 033601 (2020).
- [39] A. C. Tasolamprou, A. D. Koulouklidis, C. Daskalaki, C. P. Mavidis, G. Kenanakis, G. Deligeorgis, Z. Viskadourakis, P. Kuzhir, S. Tzortzakis, M. Kafesaki, E. N. Economou, and C. M. Soukoulis, Experimental demonstration of ultrafast THz modulation in a graphene-based thin film absorber through negative photoinduced conductivity, *ACS Photonics* **6**, 720–727 (2019).
- [40] W. Li, B. Chen, C. Meng, W. Fang, Y. Xiao, X. Li, Z. Hu, Y. Xu, L. Tong, H. Wang, W. Liu, J. Bao, and Y. R. Shen, Ultrafast all-optical graphene modulator, *Nano Lett.* **14**, 955–959 (2014).
- [41] C. T. Phare, Y.-H. D. Lee, J. Cardenas, and M. Lipson, Graphene electro-optic modulator with 30 GHz bandwidth, *Nat. Photonics* **9**, 511–514 (2015).
- [42] G. Kovacevic, C. Phare, S. Y. Set, M. Lipson, and S. Yamashita, Ultra-high-speed graphene optical modulator design based on tight field confinement in a slot waveguide, *Appl. Phys. Express* **11**, 065102 (2018).
- [43] A. B. Evlyukhin, C. Reinhardt, E. Evlyukhin, and B. N. Chichkov, Multipole analysis of light scattering by arbitrary-shaped nanoparticles on a plane surface, *J. Opt. Soc. Am. B* **30**, 2589 (2013).
- [44] S. J. Van Enk and G. Nienhuis, Commutation rules and eigenvalues of spin and orbital angular momentum of radiation fields, *J. Mod. Opt.* **41**, 963–977 (1994).
- [45] C. L. Holloway, M. A. Mohamed, E. F. Kuester, and A. Dienstfrey, Reflection and transmission properties of a metafilm: with an application to a controllable surface composed of resonant particles, *IEEE Transactions on Electromagnetic Compatibility* **47**, 853–865 (2005).